Communication

A Novel Approach to Array Manifold Calibration Using Single-Direction Information for Accurate Direction-of-Arrival Estimation

Gangil Byun and Hosung Choo

***Abstract*— A method of array manifold calibration using one steering vector measured in a single direction is proposed. The phase information of the measured steering vector is used to derive a novel calibration matrix that is proposed to compensate for the relative phase distortion (RPD) at each antenna port. We also present a metric function defined as a standard deviation of the RPD to determine the optimum calibration angle, which provides intuition for the cause of the accuracy degradation in the direction-of-arrival estimation. To verify the feasibility, a seven-element circular array with identical microstrip patch antennas is fabricated for calibrating its array manifold using a single steering vector measured in a full anechoic chamber. The calibrated array manifold is then used to estimate the direction of arrival, and its accuracy is compared to the calibrated result obtained from the traditional least-squares method. The results demonstrate that the estimation error can be improved by 54.9° compared to the traditional least-squares method, when the number of measured steering vectors is extremely limited.**

***Index Terms*— Adaptive antenna array, antenna array, array manifold calibration, direction finding array.**

I. Introduction

Array manifold calibration is essential for accurate direction-of-arrival (DoA) estimation since the existence of mutual coupling between array elements often distorts the phase information of a received signal [1]–[13]. Traditionally, this phase distortion has been compensated by adopting a least-squares calibration method that calculates a calibration matrix using the measured steering vectors obtained from different angles [14]–[21]. However, its accuracy is not guaranteed when the number of measured steering vectors is insufficient, which is a major concern for arrays mounted on huge platforms due to the inconvenience of the measurement process [22]–[25]. In addition, the number of measured steering vectors available is not generally more than one for electronic devices in mass production due to the extremely limited production time window. Thus, there has been a growing demand for a more practical approach to reducing the calibration complexity of the array manifold in case of the insufficient measurement data.

In this communication, we propose a novel approach to array manifold calibration for improved estimation accuracy using one steering vector measured in a single direction. The proposed process uses the measured phase information of a single steering vector and derives its calibration matrix using the Hadamard product between the measured steering vector and the complex conjugate of the theoretical steering vector [26]. The components of the calibration matrix represent the degree of relative phase distortion (RPD) at each antenna port, and the calibration matrix compensates for the distorted phase of theoretical steering vectors in the entire array manifold. Since the reliability of the proposed method depends on the direction of the measured steering vector, we also present a metric function defined as a standard deviation of RPD to determine the optimum calibration angle. The standard deviation of RPD also provides clear explanations of the reasons for the accuracy degradation in the DoA estimation, which allows more effective calibration without increasing the complexity.

To verify the feasibility of the proposed method, we fabricate a seven-element circular array with an inter-element spacing of a half wavelength, and its array manifold is calibrated using one measured steering vector obtained in a full anechoic chamber. The calibrated array manifold is applied to improve the root-mean-square error (RMSE) of the DoA estimation, and this calibration process is repeated by changing the direction of a measured steering vector as an enumerative investigation. In addition, the calibration accuracy of the proposed method is compared to that of the traditional least-squares method by varying the number of measured steering vectors. The result indicates that the proposed method is more efficient in improving the accuracy of DoA estimation when the measurement is limited to a few directions.

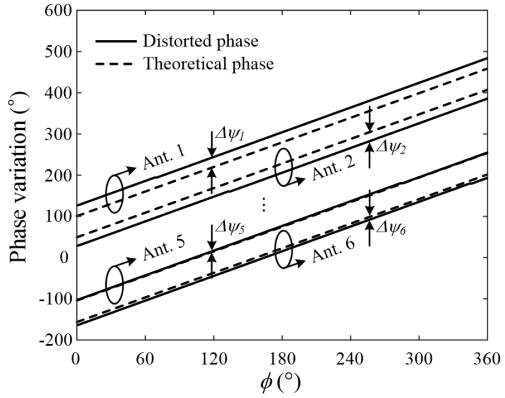

Fig. 1. Example of phase distortions for array antennas due to the mutual coupling effect.

II. Proposed Calibration Method

An array manifold is composed of steering vectors for different azimuth and elevation angles and provides a unique signature of phase information according to antenna positions and the direction of the incident wave [27]. Fig. 1 shows the example of phase variations of a seven-element uniform circular array at $\theta = 0°(0° \leq \phi \leq 360°)$. The dashed line indicates theoretical phase information with a uniform

Manuscript received January 19, 2017; revised June 2, 2017; accepted July 9, 2017. Date of publication July 24, 2017; date of current version September 1, 2017. This work was supported by the Civil Military Technology Cooperation and the Basic Science Research Program through the National Research Foundation of Korea funded by the Ministry of Education under Grant 2015R1A6A1A03031833. *(Corresponding author: Hosung Choo.)*

G. Byun is with the Metamaterial Electronic Device Research Center, Hongik University, Seoul 121-791, South Korea.

H. Choo is with the School of Electronic and Electrical Engineering, Hongik University, Seoul 121-791, South Korea (e-mail: hschoo@hongik.ac.kr).

Color versions of one or more of the figures in this communication are available online at http://ieeexplore.ieee.org.

Digital Object Identifier 10.1109/TAP.2017.2731374

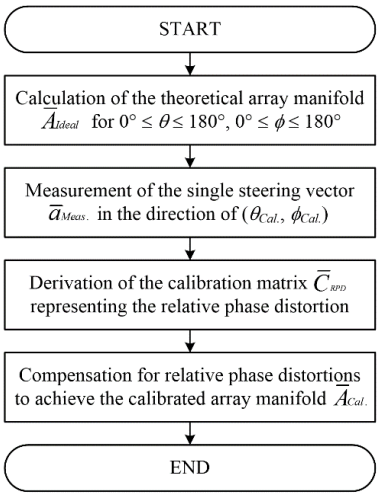

Fig. 2. Flowchart of the proposed calibration method compensating for the RPD.

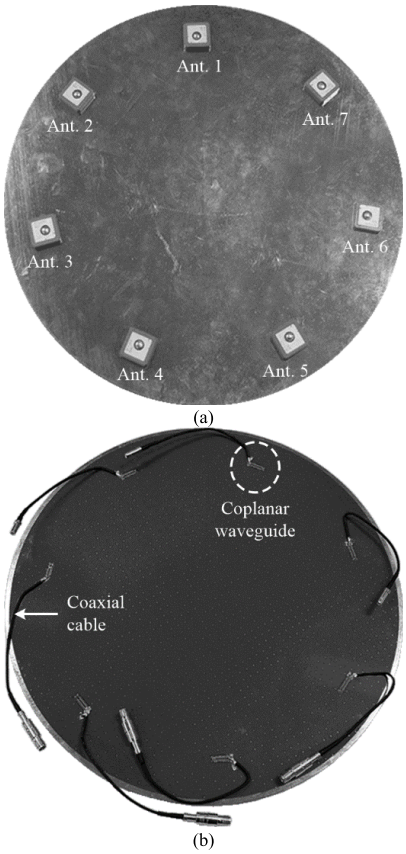

Fig. 3. Geometry of the fabricated circular array with seven off-the-shelf microstrip patch antennas. (a) Array elements with the circular ground. (b) PCB with 50-Ω coplanar waveguides and coaxial cables.

interval of 51.4°, and the solid line contains the information of phase distortions caused by the mutual coupling, which results in nonuniform phase intervals [28]. As can be seen, each antenna port experiences a different phase distortion, and the traditional least-squares method, presented in [14]–[21], compensates for this difference using the calibration matrix $\bar{C}_{\mathrm{LS}}$ as written by

$$\bar{C}_{\mathrm{LS}} = (\bar{A}_{\mathrm{Meas.}} \cdot \bar{A}^{H}_{\mathrm{Ideal}}) \cdot (\bar{A}_{\mathrm{Ideal}} \cdot \bar{A}^{H}_{\mathrm{Ideal}})^{-1} \quad (1)$$

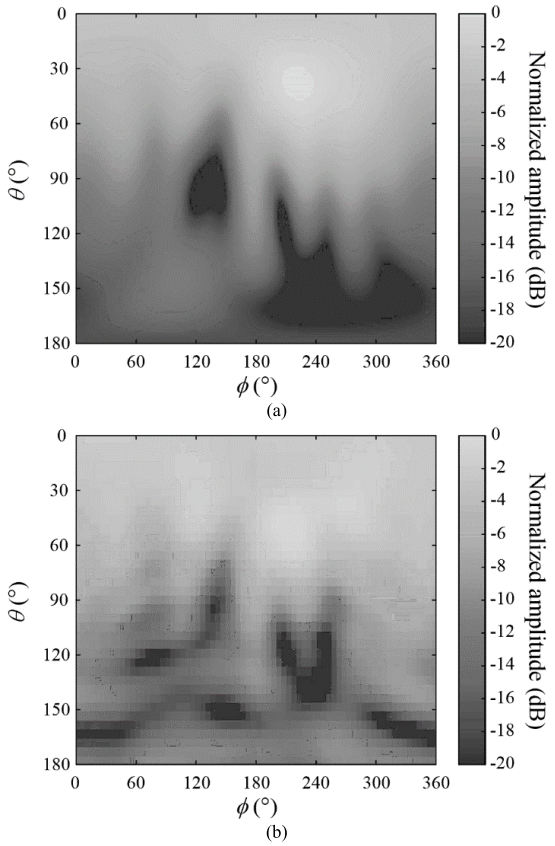

Fig. 4. Comparison of amplitude distributions obtained from E-fields of Ant. 1. (a) Simulated amplitudes. (b) Measured amplitudes.

$\bar{A}_{\mathrm{Meas.}}$ has a dimension of $N \times K$ and indicates a measured array manifold, where N is the number of antennas, and K is the number of measured steering vectors at different angles. $\bar{A}_{\mathrm{Ideal}}$ has the same matrix size of $N \times K$ and contains theoretical steering vectors that neglect the mutual coupling and platform effects. The calibration matrix $\bar{C}_{\mathrm{LS}}$ has a dimension of $N \times N$ and is adopted to obtain a calibrated array manifold $\bar{A}_{\mathrm{Cal.}}$

$$\bar{A}_{\mathrm{Cal.}} = \bar{C}_{\mathrm{LS}} \cdot \bar{A}_{\mathrm{Ideal}}. \quad (2)$$

Since the least-squares method contains an inverse operator, an insufficient number of measured steering vectors lowers the determinant value of the autocorrelation matrix of $\bar{A}_{\mathrm{Ideal}}$, which results in an inaccurately scaled matrix $\bar{C}_{\mathrm{LS}}$.

In most of the practical applications, the available number of measured steering vectors does not exceed one, thus, we propose a novel calibration matrix $\bar{C}_{\mathrm{RPD}}$ that is calculated using one measured steering vector. To prevent the inaccurate scaling, the proposed calibration matrix $\bar{C}_{\mathrm{RPD}}$ is defined using the complex conjugate and the Hadamard product without inverse matrix operation, as shown in (3), and the entire array manifold is calibrated in accordance with the proposed process specified in Fig. 2

$$\bar{C}_{\mathrm{RPD}} = \bar{a}_{\mathrm{Meas.}} \circ \bar{a}^{*}_{\mathrm{Ideal}} = [\, \Delta\psi_1 \;\; \Delta\psi_2 \;\cdots\; \Delta\psi_i \;\cdots\; \Delta\psi_N \,]^{T} \quad (3)$$

$\bar{C}_{\mathrm{RPD}}$ has a dimension of $N \times 1$, and $\bar{a}_{\mathrm{Meas.}}$ and $\bar{a}_{\mathrm{Ideal}}$ are the vector components of $\bar{A}_{\mathrm{Meas.}}$ and $\bar{A}_{\mathrm{Ideal}}$, respectively. Each element of $\bar{C}_{\mathrm{RPD}}$ represents the RPD, denoted as $\Delta\psi_1$, $\Delta\psi_2 \ldots \Delta\psi_7$, and the RPD is calculated as

$$\Delta\psi_i = \psi_{\mathrm{Meas.,i}} - \psi_{\mathrm{Ideal,i}} \quad (4)$$

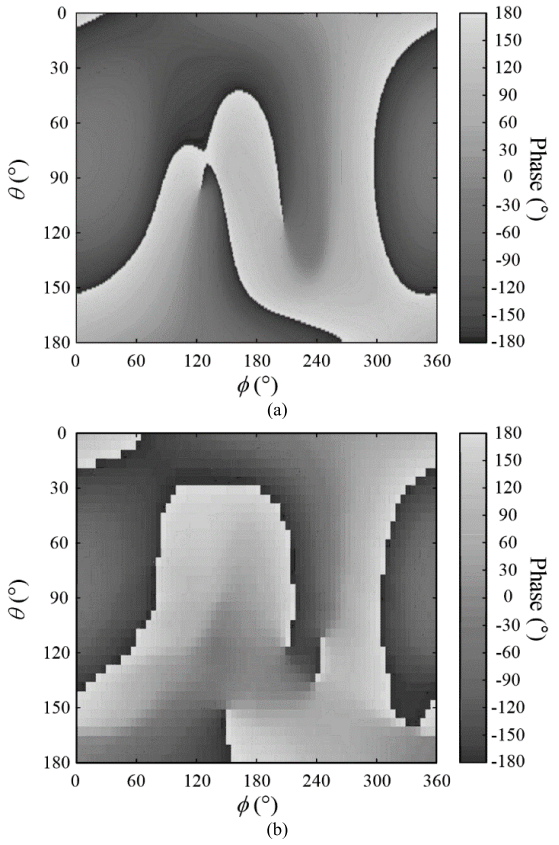

Fig. 5. Comparison of phase distributions obtained from E-fields of Ant. 1. (a) Simulated phases. (b) Measured phases.

where i is an element index, and the minus operator comes from the complex conjugate in (3). $\bar{A}_{\text{Ideal}}$ is calibrated through the Hadamard product using the matrix with K columns of $\bar{C}_{\text{RPD}}$, and the resulting calibrated array manifold is denoted by $\bar{A}_{\text{Cal.}}$

$$\bar{A}_{\text{Cal.}} = \underbrace{[\,\bar{C}_{\text{RPD}} \cdots \bar{C}_{\text{RPD}}\,]}_{K \text{ columns}} \circ \bar{A}_{\text{Ideal}} \tag{5}$$

$\bar{A}_{\text{Cal.}}$ is then applied for the DoA estimation using a conventional MUSIC algorithm [29] shown in (6), and the MUSIC spectrum $\bar{P}_{\text{MUSIC}}$ is scanned in both elevation θ and azimuth ϕ

$$\bar{P}_{\text{MUSIC}}(\theta,\phi) = \frac{\bar{a}_{\text{Cal.}}(\theta,\phi)^H \cdot \bar{a}_{\text{Cal.}}(\theta,\phi)}{\bar{a}_{\text{Cal.}}(\theta,\phi)^H \cdot \bar{U}_n \cdot \bar{U}_n^H \cdot \bar{a}_{\text{Cal.}}(\theta,\phi)} \tag{6}$$

$\bar{a}_{\text{Cal.}}$ is the vector component of $\bar{A}_{\text{Cal.}}$, and $(\cdot)^H$ refers to the Hermitian transpose, which is a conjugate transpose. $\bar{U}_n$ indicates the noise subspace and is obtained from an eigenvalue decomposition of a covariance matrix $\bar{R}$ that is defined by

$$\bar{R} = \bar{x} \cdot \bar{x}^H \tag{7}$$

where $\bar{x}$ is the time-domain signal received by array antennas. The peak direction of the MUSIC spectrum is written as $\phi_{\text{Est.}}$ and $\theta_{\text{Est.}}$ for azimuth and elevation, respectively, and is used to compute an RMSE as

$$\text{RMSE}(^\circ) = \sqrt{(\phi_{\text{True}} - \phi_{\text{Est.}})^2 + (\theta_{\text{True}} - \theta_{\text{Est.}})^2} \tag{8}$$

for a true signal direction of ϕ_{True} and θ_{True}.

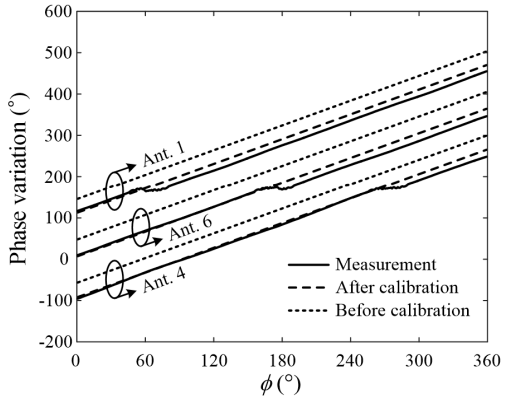

Fig. 6. Phase variations of Ant. 1, Ant. 4, and Ant. 6 at $\theta = 0^\circ$ before and after the array manifold calibration.

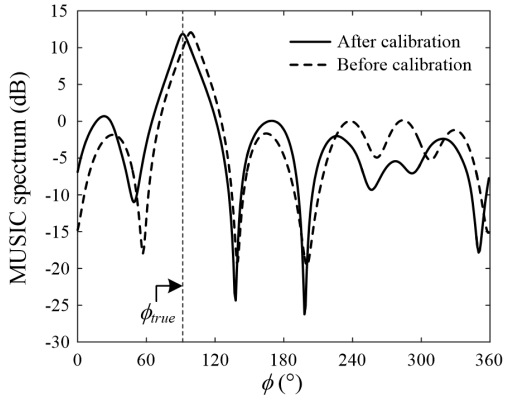

Fig. 7. Comparison of MUSIC spectrums showing the effectiveness of the calibration when a source is placed at $\phi_{\text{True}} = 90^\circ$.

III. Measurement and Analysis

A. Antenna Characteristics of the Seven-Element Array

Fig. 3(a) shows a photograph of a fabricated array with seven microstrip patch antennas, and their inter-element spacing is approximately a half wavelength. Each antenna has a square patch with an edge length of 12.8 mm, and the patch is fed by a coaxial probe at 1.1 mm off the center [30]. The size is reduced by printing the patch on a high-dielectric ceramic substrate ($\varepsilon_r = 40$, $\tan\delta = 0.0035$) with a thickness of 4 mm, and its two corners are truncated by 1.3 mm for circular polarization. Fig. 3(b) is a bottom view of the array and shows a printed circuit board (PCB) integrating 50-Ω coplanar waveguides as transmission lines.

An array manifold of the fabricated array is obtained from the amplitude and phase of far-zone fields measured in a full anechoic chamber. Fig. 4 illustrates a comparison of simulated and measured amplitudes at Ant. 1. The peak amplitude is slightly steered toward a lower elevation angle of $\theta = 50^\circ$ and $\phi = 210^\circ$ for both results due to antenna placement on a finite ground platform. Fig. 5 shows that the phase is more sensitive to mutual coupling and platform effects; for instance, the maximum RPD of 179.7° is observed at $\phi = 155^\circ$ and $\theta = 115^\circ$.

Fig. 6 presents the phase variations as a function of ϕ at the boresight direction ($\theta = 0$) for Ant. 1, Ant. 4, and Ant. 6. A solid line indicates a measured phase variation, while a dotted line represents a theoretical variation. The theoretical result has an equivalent phase interval of about 102.9°; on the other hand, the measured phase intervals are nonuniform due to the effect of mutual coupling and

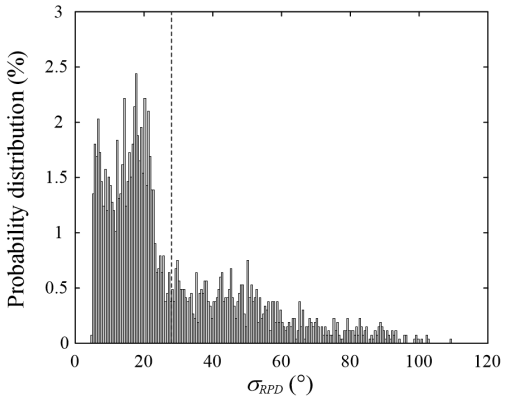

Fig. 8. Probability distributions of the proposed metric values calculated from steering vectors measured with an angular interval of 5°.

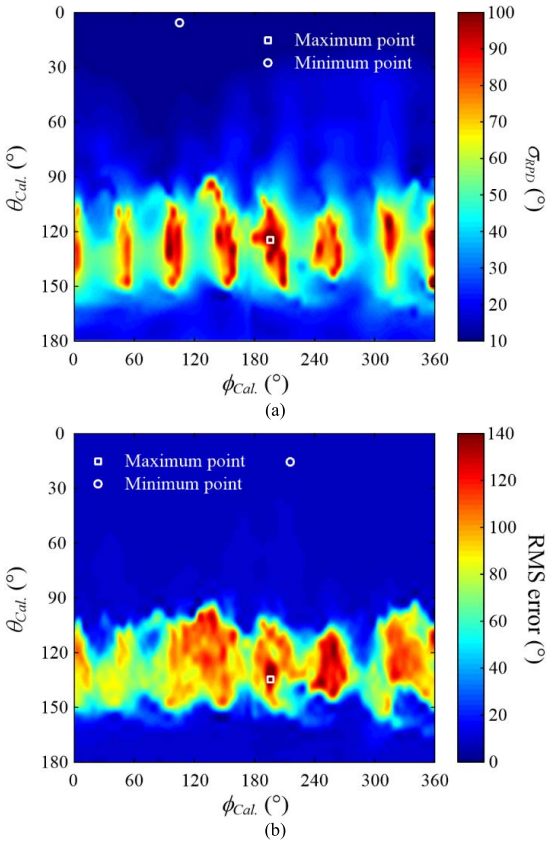

Fig. 9. Complete enumeration investigation of σ_{RPD} and the RMSE in both azimuth and elevation. (a) Angular distributions of σ_{RPD}. (b) Angular distributions of the estimation error.

platforms. This distorted phase interval of each antenna can be compensated using the proposed calibration matrix $\bar{C}_{\mathrm{RPD}}$, and the result is specified by a dashed line. Note that nonlinear phase distributions at around $\phi = 60°$, $\phi = 270°$, $\phi = 180°$ for Ant. 1, Ant. 4, and Ant. 6, respectively, are caused because the actual direction of measurement is slightly off the phase center.

Fig. 7 shows the effectiveness of this calibrated phase variation in terms of the MUSIC spectrum. The peak values of the solid and dashed lines are observed at $\phi_{\mathrm{Est.}} = 92°$ and $\phi_{\mathrm{Est.}} = 99°$ with values of 11.9 and 12.1 dB, respectively, when the true direction ϕ_{True} is 90°. This result implies that the proposed method can improve the RMSE

TABLE I

RANGE OF RMSE FOR CLUSTERING σ_{RPD} VALUES AS THE ENUMERATIVE INVESTIGATION

Classification	Range
RMSE #1	0° ≤ RMSE < 8°
RMSE #2	8° ≤ RMSE < 10°
RMSE #3	10° ≤ RMSE < 20°
RMSE #4	20° ≤ RMSE < 40°
RMSE #5	40° ≤ RMSE

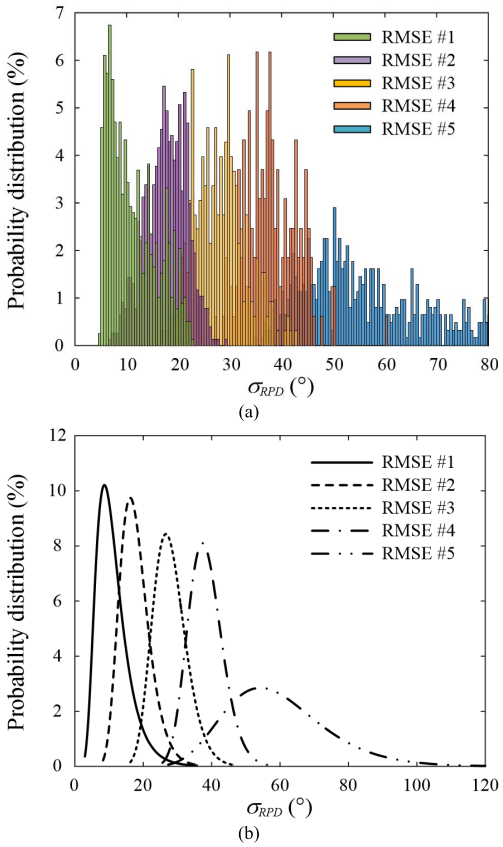

Fig. 10. Probability distributions of σ_{RPD} divided into groups. (a) Probability distributions with bars. (b) Fit log-normal distributions.

by compensating for the RPD using one steering vector measured in a single direction.

B. Optimum Calibration Angle and Analysis

To better understand the optimum angle of calibration, a standard deviation of RPD is defined as a metric function and is denoted as

$$\sigma_{\mathrm{RPD}} = \mathrm{std}\{\mathrm{RPD}\} = \sqrt{\frac{1}{N-1}\sum_{n=1}^{N} |\Delta\psi_n - \mu_{\mathrm{RPD}}|^2} \tag{9}$$

where μ_{RPD} represents the mean RPD of $\bar{C}_{\mathrm{RPD}}$ that is calculated by

$$\mu_{\mathrm{RPD}} = \frac{1}{N}\sum_{n=1}^{N} \Delta\psi_n. \tag{10}$$

As an enumerative investigation, σ_{RPD} is computed for all steering vectors measured at an angular interval of 5°, which produces 2664 values. Fig. 8 presents a probability distribution of the entire

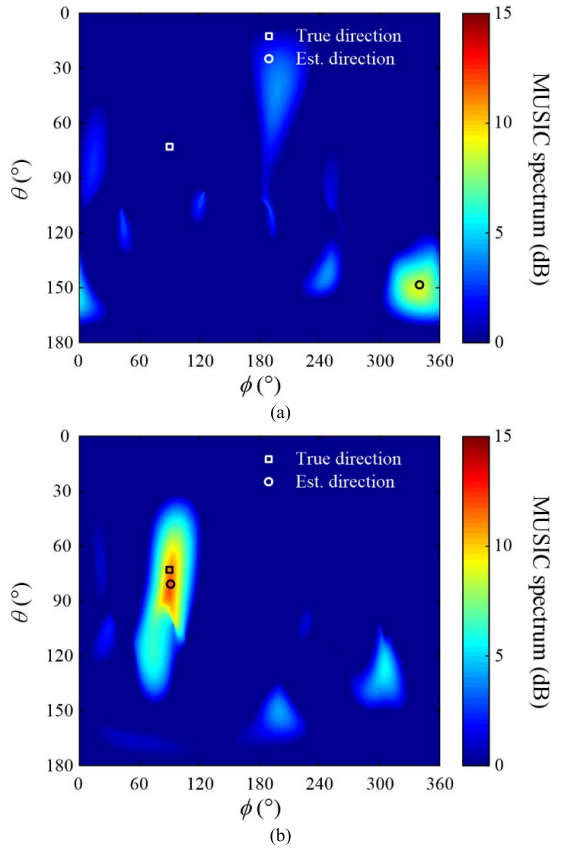

Fig. 11. Comparison of MUSIC spectrums after calibrating the array manifold using measured steering vectors with different σ_{RPD} values. (a) Calibration result using the maximum σ_{RPD} value of 110°. (b) Calibration result using the minimum σ_{RPD} value of 5°.

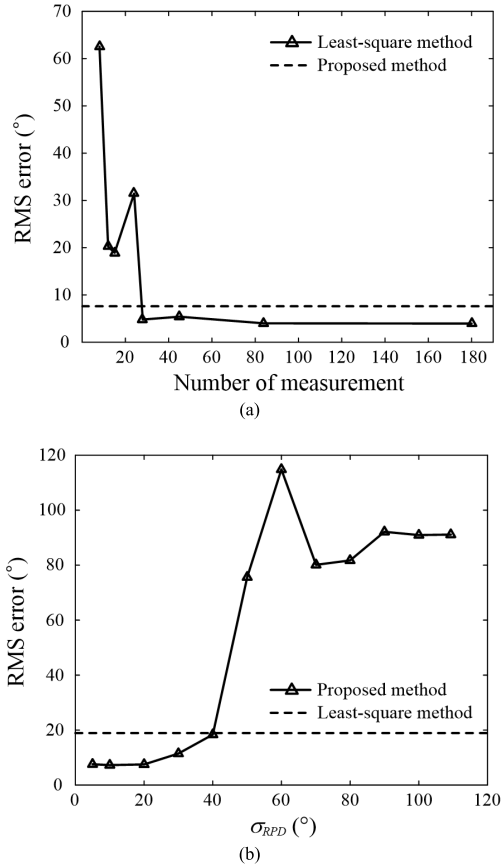

Fig. 12. Comparison of the RMSE between the proposed method and the traditional least-squares calibration method. (a) Variation of the RMSE of the traditional least-squares calibration method according to the number of measured steering vectors. (b) Variation of the RMSE of the proposed method according to σ_{RPD}.

σ_{RPD} values, and the RMSE that corresponds to each σ_{RPD} is calculated to analyze an interaction. It is assumed that the noise level is -90 dBm and the signal-to-noise ratio is about 30 dB. We calculate the RMSE for DoAs from $\phi_{\text{True}} = 0°$ to $\phi_{\text{True}} = 350°$ at an interval of 10° and obtain more reliable average values by iterating this process 100 times. Fig. 9(a) and (b) shows the distributions of σ_{RPD} and the RMSE according to the angle of the measured steering vector. The values of σ_{RPD} tend to increase at low elevation angles, and a similar trend can also be observed in the distribution of the RMSE. For a more intuitive analysis, the RMSE is divided into five subranges, as listed in Table I, and σ_{RPD} values are classified by their RMS values. Note that the specific values of the five subranges are empirically determined, and the five groups contain 620, 162, 327, 769, and 786 data. Fig. 10(a) shows the probability distributions of the classified groups that are specified by different colors, and each distribution is also fit to a log-normal distribution, as shown in Fig. 10(b). The peak positions of the log-normal distributions are observed at 8.9°, 16.3°, 26.6°, 37.7°, and 54.1° and tend to shift toward larger σ_{RPD} values as the group includes larger RMSE values. Thus, accurate DoA estimation can be achieved when σ_{RPD} values are included within a range between 5° and 12.8°, in other words, the individual elements of an array should experience a similar phase distortion for optimum calibration.

Fig. 11 shows the example of MUSIC spectrums, when a signal is located at $\phi_{\text{True}} = 90°$ and $\theta_{\text{True}} = 75°$. Fig. 11(a) is obtained from $\bar{A}_{\text{Cal.}}$ that is calibrated using the measured steering vector with a σ_{RPD} value of 109.3° in the direction of $\phi_{\text{Cal.}} = 195°$ and $\theta_{\text{Cal.}} = 125°$. The peak value of the spectrum appears at $\phi_{\text{Est.}} = 339°$ and $\theta_{\text{Est.}} = 151°$, and its RMSE is 184.1°. Another spectrum, presented in Fig. 11(b), is calculated using a calibration vector measured at $\phi_{\text{Cal.}} = 105°$ and $\theta_{\text{Cal.}} = 5°$, and the σ_{RPD} value of the measured steering vector is reduced to 5°. As can be seen, the RMSE is drastically improved by 178.4°, and this error improvement can be anticipated by observing the reduced value of σ_{RPD}.

The suitability of the proposed method is further investigated by comparing the variation of the average RMSE with the traditional least-squares method, and a different number of measured steering vectors is employed to calibrate the array manifold of the seven-element array, as presented in Fig. 12(a). The traditional method maintains the RMSE to be less than 5° when the number of measured steering vectors is greater than 24; however, it is significantly increased to 62.5° in the case of fewer measurements. Although enough number of measured steering vectors enables the traditional least-squares method to have better performances, the inverse operator used in the computation of $\bar{C}_{\text{LS}}$ causes irregular amplitude scaling for a fewer number of measured steering vectors. For example, the scaling factor significantly increases from 2.4×10^{-16} to 2.3×10^{6} when the number decreases from 180 to 12. On the other hand, the proposed method maintains the average RMSE of 7.6°, which becomes lower than that of the traditional method when the number of measured steering vectors is less than 24. We further observed variations of the RMSE for different σ_{RPD}, as shown in Fig. 12(b), and detailed information on the measured steering vectors used in this approach is listed

TABLE II
DETAILED INFORMATION OF THE MEASURED STEERING VECTORS USED IN THE PROPOSED METHOD

Index	$\theta_{Cal.}$	$\phi_{Cal.}$	σ_{RPD}
1	180°	105°	5°
2	170°	275°	10°
3	130°	300°	20°
4	85°	100°	30°
5	75°	40°	40°
6	80°	320°	50°
7	60°	330°	60°
8	40°	50°	70.1°
9	60°	55°	80°
10	45°	160°	90°
11	55°	95°	100°
12	60°	195°	109.3°

in Table II. The directions of these measured steering vectors, denoted as $\theta_{\mathrm{Cal}.}$ and $\phi_{\mathrm{Cal}.}$, are determined by searching corresponding σ_{RPD} values from 5° to 109.3°. These results are then compared to the RMSE of the least-squares method calculated using twelve measured steering vectors, which is the first data point in Fig. 12(a). As can be seen, the proposed method is feasible to maintain lower RMSE compared to the least-squares method, when σ_{RPD} is smaller than 40°.

IV. CONCLUSION

We investigated the method of array manifold calibration using one steering vector measured in a single direction for improved estimation accuracy. To avoid the inaccurate-scaling issue of the traditional least-squares calibration method, we defined the calibration matrix using only the complex conjugate and the Hadamard product without the inverse operator. We also presented the metric function, defined as a standard deviation of RPD, to determine the optimum calibration angle with low complexity and to better explain the reason of the increased RMSE in the proposed calibration process. The suitability was then verified using the fabricated seven-element array by observing its average RMSE after calibration, and the result was compared to the traditional method by varying the number of measured steering vectors for calibration. As a result, the RMSE was significantly improved from 62.5° to 7.6°, when the number of measured steering vectors is restricted to less than 24.

REFERENCES

[1] J. Rubio, J. F. Izquierdo, and J. Córcoles, "Mutual coupling compensation matrices for transmitting and receiving arrays," *IEEE Trans. Antennas Propag.*, vol. 63, no. 2, pp. 839–843, Feb. 2015.

[2] H.-S. Lui and H. T. Hui, "Direction-of-arrival estimation: Measurement using compact antenna arrays under the influence of mutual coupling," *IEEE Antennas Propag. Mag.*, vol. 57, no. 6, pp. 62–68, Dec. 2015.

[3] B. H. Wang and H. T. Hui, "Wideband mutual coupling compensation for receiving antenna arrays using the system identification method," *IET Microw., Antennas Propag.*, vol. 5, no. 2, pp. 184–191, Jan. 2011.

[4] H.-S. Lui and H. T. Hui, "Improved mutual coupling compensation in compact antenna arrays," *IET Microw., Antennas Propag.*, vol. 4, no. 10, pp. 1506–1516, Oct. 2010.

[5] K. R. Dandekar, H. Ling, and G. Xu, "Effect of mutual coupling on direction finding in smart antenna applications," *Electron. Lett.*, vol. 36, no. 22, pp. 1889–1891, Oct. 2000.

[6] H. T. Hui, "Improved compensation for the mutual coupling effect in a dipole array for direction finding," *IEEE Trans. Antennas Propag.*, vol. 51, no. 9, pp. 2498–2503, Sep. 2003.

[7] K. R. Dandekar, H. Ling, and G. Xu, "Experimental study of mutual coupling compensation in smart antenna applications," *IEEE Trans. Wireless Commun.*, vol. 1, no. 3, pp. 480–487, Jul. 2002.

[8] Q. Bao, C. C. Ko, and W. Zhi, "DOA estimation under unknown mutual coupling and multipath," *IEEE Trans. Aerosp. Electron. Syst.*, vol. 41, no. 2, pp. 565–573, Apr. 2005.

[9] C. M. S. See, "Sensor array calibration in the presence of mutual coupling and unknown sensor gains and phases," *Electron. Lett.*, vol. 30, no. 5, pp. 373–374, Mar. 1994.

[10] A. P.-C. Ng, "Direction-of-arrival estimates in the presence of wavelength, gain, and phase errors," *IEEE Trans. Signal Process.*, vol. 43, no. 1, pp. 225–232, Jan. 1995.

[11] D. F. Kelley and W. L. Stutzman, "Array antenna pattern modeling methods that include mutual coupling effects," *IEEE Trans. Antennas Propag.*, vol. 41, no. 12, pp. 1625–1632, Dec. 1993.

[12] B. Friedlander and A. J. Weiss, "Direction finding in the presence of mutual coupling," *IEEE Trans. Antennas Propag.*, vol. 39, no. 3, pp. 273–284, Mar. 1991.

[13] I. J. Gupta and A. A. Ksienski, "Effect of mutual coupling on the performance of adaptive arrays," *IEEE Trans. Antennas Propag.*, vol. AP-31, no. 5, pp. 785–791, Sep. 1983.

[14] C. Liang and F. Wen, "Received signal strength-based robust cooperative localization with dynamic path loss model," *IEEE Sensors J.*, vol. 16, no. 5, pp. 1265–1270, Mar. 2016.

[15] B. Liao, J. Wen, L. Huang, C. Guo, and S.-C. Chan, "Direction finding with partly calibrated uniform linear arrays in nonuniform noise," *IEEE Sensors J.*, vol. 16, no. 12, pp. 4882–4890, Jun. 2016.

[16] S. D. Blunt, T. Chan, and K. Gerlach, "Robust DOA estimation: The reiterative superresolution (RISR) algorithm," *IEEE Trans. Aerosp. Electron. Syst.*, vol. 47, no. 1, pp. 332–346, Jan. 2011.

[17] M.-Y. Lee and C. Yoo, "Gain and phase mismatch calibration technique in image-reject RF receiver," *J. Electromagn. Eng. Sci.*, vol. 10, no. 1, pp. 25–27, Mar. 2010.

[18] M. A. Koerber and D. R. Fuhrmann, "Array calibration by Fourier series parameterization: Scaled principal components method," in *Proc. IEEE Int. Conf. Acoust., Speech, Signal Process.*, vol. 4. Apr. 1993, pp. 340–343.

[19] J. Pierre and M. Kaveh, "Experimental performance of calibration and direction-finding algorithms," in *Proc. IEEE Int. Conf. Acoust., Speech, Signal Process.*, vol. 2. Apr. 1991, pp. 1365–1368.

[20] G. H. Golub and V. Pereyra, "The differentiation of pseudo-inverses and nonlinear least squares problems whose variables separate," *SIAM J. Numer. Anal.*, vol. 10, no. 2, pp. 413–432, Feb. 1973.

[21] R. S. Adve and T. K. Sarkar, "Compensation for the effects of mutual coupling on direct data domain adaptive algorithms," *IEEE Trans. Antennas Propag.*, vol. 48, no. 1, pp. 86–94, Jan. 2000.

[22] G. Byun, H. Choo, and H. Ling, "Optimum placement of DF antenna elements for accurate DOA estimation in a harsh platform environment," *IEEE Trans. Antennas Propag.*, vol. 61, no. 9, pp. 4783–4791, Sep. 2013.

[23] S. D. Keller, "Wire-frame monocone antenna for direction-finding applications on unmanned aerial vehicle platform," *IEEE Antennas Propag. Mag.*, vol. 53, no. 1, pp. 56–65, Feb. 2011.

[24] T. Su and H. Ling, "Array beamforming in the presence of a mounting tower using genetic algorithms," *IEEE Trans. Antennas Propag.*, vol. 53, no. 6, pp. 2011–2019, Jun. 2005.

[25] F. Obelleiro, L. Landesa, J. M. Taboada, and J. L. Rodriguez, "Synthesis of onboard array antennas including interaction with the mounting platform and mutual coupling effects," *IEEE Antennas Propag. Mag.*, vol. 43, no. 2, pp. 76–82, Apr. 2001.

[26] R. A. Horn and C. R. Johnson, *Matrix Analysis*, 2nd ed. Cambridge, U.K.: Cambridge Univ. Press, 2012.

[27] C. A. Balanis, *Antenna Theory: Analysis and Design*, 4th ed. New York, NY, USA: Wiley, 2016, pp. 283–284.

[28] B. C. Ng and C. M. S. See, "Sensor-array calibration using a maximum-likelihood approach," *IEEE Trans. Antennas Propag.*, vol. 44, no. 6, pp. 827–835, Jun. 1996.

[29] R. O. Schmidt, "Multiple emitter location and signal parameter estimation," *IEEE Trans. Antennas Propag.*, vol. AP-34, no. 3, pp. 276–280, Mar. 1986.

[30] Amotech Co. Ltd. (2015). *Ceramic Patch Antenna Model: B25-2D02753-STD70.* [Online]. Available: http://www.amotech.co.kr